Multiscale modeling of biomechanical properties of red blood cells

A. S. Ademiloye[a,b,*], Jorge Molina[c], Mohammad Abughabush[a], Yang Zhang[d], Ping Xiang[e]

[a]Zienkiewicz Institute for Modelling, Data and AI, Faculty of Science and Engineering, Swansea University, Bay Campus, Swansea, UK
[b]Department of Biomedical Engineering, Faculty of Science and Engineering, Swansea University, Bay Campus, Swansea, UK
[c]Esc. Ing. Caminos, Campus Fuentenueva, University of Granada, Granada, Spain
[d]School of Physics, Nanjing University of Science and Technology, Nanjing, 210094, China
[e]School of Civil Engineering, Central South University, Changsha, 410075, Hunan, China

Abstract

In recent decades, the biomechanical and biophysical properties of human red blood cells (RBCs) have been greatly explored by numerous researchers for diverse reasons. In normal physiological conditions, RBCs undergo large deformation when traversing thin microcapillaries, however, upon infection by different blood-related diseases such as malaria, sickle cell anemia and diabetes mellitus, they experience impaired deformability. Several experimental and numerical techniques have been proposed to elucidate the primary reasons for the observed impaired deformability and increased stiffening of RBC membrane. Multiscale modelling as a candidate numerical technique for this purpose is of particular interest since it incorporates more intrinsic details such as cellular architecture, microscale defects and substructural changes into its constitutive formulation, often resulting to improved accuracy and better computational efficiency. This chapter discusses some of the recent advances in multiscale modelling of the biomechanical properties of red blood cells. These advances include, among many others, efforts to accurately predict the biomechanical properties of healthy and diseased RBCs using a multiscale meshfree modelling framework. It also provides insights into how microstructural and temperature changes influence their deformability, pathogenesis, and pathophysiology. Furthermore, some perspectives on the multiscale modelling of biomechanical behaviors of RBCs are presented.

---

[*] Corresponding author email: a.s.ademiloye@swansea.ac.uk (A.S. Ademiloye)

1. Introduction

Hematological fluid in animals, known as blood, serves the vital function of conveying essential elements like nutrients and oxygen to cells while carrying away metabolic byproducts from these cells. This intricate and distinctive fluid can be conceptualized as a blend of Red Blood Cells (RBCs) or erythrocytes, White Blood Cells (WBCs) or leukocytes, platelets, and blood plasma within a non-Newtonian fluid. Particulate constituents, especially RBCs, make up over 99% of the material in blood, contributing to approximately 40-45% of its volume (Klöppel & Wall, 2011). Furthermore, indications point to the fact that the characteristics and conditions of the cells play a crucial role in shaping the collective behavior of the blood.

RBCs are biconcave, elastic, and non-nucleated, with diameter and thickness of about 8 μm and 2.5 μm, respectively. The main component of their membrane is a fluid-like lipid bilayer that is fundamental to resisting bending. Additionally, there is an interconnected cytoskeleton based on spectrin, which not only helps maintain the cell's shape but also aids in its mobility. The connections between the lipid bilayer and spectrin domains are facilitated by transmembrane proteins. Specifically, the cytoskeleton structure of the RBC membrane can be described as a two-dimensional (2D) hexagonal arrangement, comprising spectrin tetramers and actin complexes (Pan et al., 2018). Biomechanical properties of the membrane are widely recognized as vital for maintaining cellular functions due to its large reversible deformation capability while traversing vessels during microcirculation. Nevertheless, deviations in these properties are intricately associated with various physiological and pathological processes, potentially leading to the development of diverse blood-related diseases, whether hereditary or non-hereditary.

Among these, malaria stands out as one of the most significant blood-related infections, which claims the lives of more children worldwide than any other infectious disease. According to the World Malaria Report 2024 published by the World Health Organization, approximately 263 million new cases of malaria (range 238–294 million) and 597,000 malaria deaths (range 548,000–723,000) were reported worldwide in 2023, with the African region accounting for most global cases (up to 94%). Following invasion by the malaria parasite, the host's RBC membrane experiences a diminished deformability and a reduced capability to regain its initial shape when subjected to fluid shear stress in vitro (Cranston et al., 1984). This alteration leads to a notable elevation in shear modulus, rigidity, and cell viscosity (Suresh, 2006), causing an impediment in the microcirculation process. Consequently, this disruption contributes to the dysfunction of various organs within the human body. In spite of the progress in understanding malaria pathogenesis, the primary mechanism responsible for the loss of deformability remains unclear.

To understand this phenomenon, numerous experimental methods have been proposed to analyze and mimic the behavior, motion, and deformation of healthy and diseased RBCs within microcapillaries. Previous studies in literature have shown that the deformability of the red blood cell (RBC) can be assessed in terms of its membrane elastic and mechanical behaviors. This achievement was realized through various experimental techniques, including atomic force microscopy (Dulińska et al., 2006; Kuznetsova et al., 2007), micropipette aspiration (Chien et al., 1978; Evans, 1973), RBC edge flicker microscopy (Strey et al., 1995), microfluidic experiments (Franke et al., 2011; Quinn et al., 2011), tracking of fluorescent nanometer beads attached to RBCs (Lee & Discher, 2001) and RBC deformation by optical tweezers (Henon et al., 1999; Lenormand et al., 2001; Dao et al., 2003; Mills et al., 2004; Tan et al., 2009).

Nevertheless, computational models have been developed in recent years as a promising way for studying the structural, mechanical, and rheological properties of RBCs both in health and disease. These numerical approaches can be categorized as particle-based, continuum-based, and multiscale models. In particle-based methods, the RBC membrane structure is depicted using a network of springs and particulate assembly. The key benefit lies in the straightforward mathematical representation, enabling the avoidance of intricate solid mechanics formulations in their numerical implementations. Nevertheless, the spring constant values are empirical, and the mechanical properties are highly influenced by the configuration of the network (Imai et al., 2016). Discher and colleagues (Discher et al., 1998) examined several elastic characteristics of the RBC spectrin network. They identified three structural models, specifically the stress-free model, the prestress model, and the condensed model. Additionally, the utilization of particle-based techniques, such as the approach associated with coarse-grained molecular dynamics (Li et al., 2005), dissipative particle dynamics (Pivkin et al., 2008; Fedosov et al., 2020), the moving particle method (Tsubota et al., 2006; Ahmadian et al., 2011), the lattice Boltzmann method (Krüger et al., 2011), and the smoothed particle hydrodynamics (SPH) method (Hosseini and Feng, 2009), has been extensively explored for diverse investigations into RBC properties.

On the other hand, within continuum-based techniques, the membrane is discretized through a triangular mesh, where the equations of solid mechanics governing the membrane are solved. This method proves valuable for determining membrane tension in the presence of fluid flow. Nevertheless, it frequently suffers from numerical instabilities stemming from membrane compression. Various researchers have endeavored to incorporate a bending resistance into the model to counteract this instability, but a conclusive solution has not been reached to date. Among all the existing state-of-the-art literature, it could be highlighted that the work of Hansen et al., (1996) established a continuum model for predicting the bulk elastic shear modulus and the area expansion modulus of RBC membranes. In this line, Dao and co-workers (Dao et al., 2003) studied the deformation behavior of a single RBC by simulating the optical tweezers experiment using the finite element method, and Besides, Klöppel and Wall (Klöppel and Wall, 2011) developed a novel two-layer, coupled finite element approach for modelling the nonlinear elastic and viscoelastic behavior of RBC membrane.

Finally, in multiscale-based models, the benefits of atomistic simulation and continuum modelling are integrated. This involves utilizing a particle-based model to calculate biomechanical properties of the membrane, such as strain energy density, stress tensors, and tangent modulus matrix (Ademiloye, 2017). Subsequently, these computed parameters are utilized to establish the constitutive material response, which is then applied in numerical simulations within the framework of continuum mechanics. As an example of this approach, Dupin and his colleagues (Dupin et al, 2007) implemented a 3D Lattice Boltzmann Method to investigate the dynamics of healthy, malaria-infected, and sickle RBCs. They modelled the elastic properties of the cell membrane as a network of springs and represented the surrounding fluid using a Eulerian Navier-Stokes solver. A different course of action was proposed by Fedosov et al. (2011), who employed a dissipative particle dynamics (DPD) method to model both RBC mechanics and surrounding flow. Hartmann (2010) used a multiscale model to simulate optical tweezers experiments to study mechanical properties of RBC.

Ademiloye and co-workers (Ademiloye et al., 2015) developed a 2D atomistic-continuum model based on the higher-order Cauchy-Born rule. This work improved the previous studies in literature (Wang et al., 2014) by considering all energy contributions in the RBC membrane and subsequently studied the effect of area and volume constraint coefficients on the elastic and mechanical properties of RBC membrane. To extend the utility of the proposed approach for large deformation studies on the RBC membrane, a new formulation that models the RBC as a 2D surface within a 3D space whilst accounting for the precise membrane thickness has also been proposed (Ademiloye et al., 2017; Ademiloye et al., 2018). More recently, Ma et al. (2022) employed a two-step multiscale computational framework based on coarse-grained molecular dynamics to probe the viscoelastic properties of the surface-altered RBCs in aging and mechanical fatigue.

In the remaining section of this chapter, we focus on modelling the biomechanical properties of RBC membrane in healthy and diseased conditions based on a three-dimensional (3D) multiscale meshfree framework.

2. Method and Models

2.1. RBC Membrane Structural Model Description

The RBC membrane structural model is defined based on the microstructural pattern of its underlying spectrin cytoskeletal network, in which a representative cell is selected as a symmetrical hexagon. The selected representative cell is composed of seven junction complexes and six spectrin links. All spectrin links in the representative cell are assumed to have the same initial length L_i, persistence length p and maximum contour length L_{max} at any point in time, as shown in Fig. 1 below.

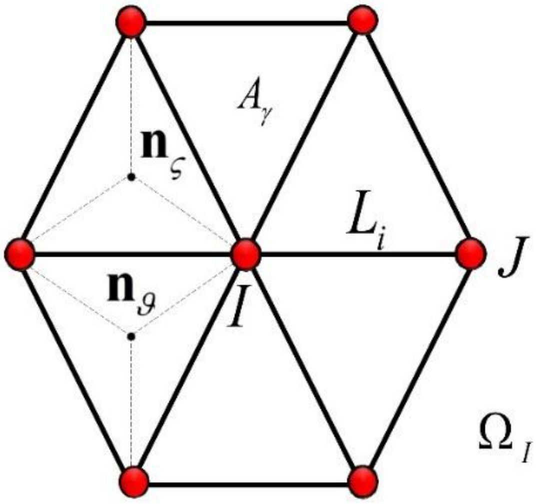

Figure 1. Representative cell of the RBC membrane showing junction complex I, spectrin link length L_i and area Ω_I. A_γ is the area of triangle plaquette formed by three vertexes. The membrane bending energy $E_{bending}$ due to two adjacent triangle plaquettes can be defined in term of an instantaneous curvature angle $\theta_{\varsigma\vartheta}$ using normal vectors $\mathbf{n}_\varsigma$ and $\mathbf{n}_\vartheta$ (Source: Ademiloye et al., 2017, permission requested)

2.2. Multiscale Cauchy-Born RBC Model

The construction of a 3D multiscale hyperelastic constitutive model based on the first-order Cauchy-Born rule (Tadmor et al., 1999) is concisely presented. The first-order Cauchy-Born rule was utilized to derive the continuum material properties based on an underlying atomistic model in a physically consistent way such that the relationship between the deformed and undeformed lattice vector between two nodes in terms of the first-order deformation gradient tensor is defined as follows:

$$\boldsymbol{r}_{IJ} \approx \boldsymbol{Grad} \cdot R_{IJ}, \tag{1}$$

where $\mathbf{Grad} = G_{iJ} e_i \otimes e_J$, and $\boldsymbol{R}_{IJ}$ denote the first-order deformation gradient tensor and the undeformed lattice vector in the material configuration, respectively. The corresponding lattice vector in the deformed configuration is represented by $\boldsymbol{r}_{IJ}$ (or L_i). In addition, the first-order deformation gradient tensor $\boldsymbol{Grad}$ can be defined as $\boldsymbol{Grad}(i, J) = \frac{\partial \boldsymbol{x}}{\partial \boldsymbol{X}}$, where $i, J = 1,2,3$. $\boldsymbol{X} = (X_1, X_2, X_3)$ is the coordinate of a nodal point in the material configuration, and $\boldsymbol{x} = (x_1, x_2, x_3)$ denotes its corresponding spatial position after the application of external loading.

The strain energy density function (W_T) corresponding to the energy at a junction complex I in the representative cell is computed as a function of the total coarse-grained Helmholtz free energy density (Wang et al., 2014; Ademiloye et al., 2015), assumed membrane thickness, h_o, and average area per junction complex in the original configuration, Ω_I, calculated using $\frac{\sqrt{3} L_i{}^2}{2}$. This can be expressed mathematically as follows:

$$W_T = W_T(\boldsymbol{Grad}) = \frac{h_o}{\Omega_I} V_I = \frac{h_o}{\Omega_I} \left[\frac{1}{2} \sum_{J=1}^{6} E_{\mathrm{WLC}}\,(\boldsymbol{r}_{IJ}) + \frac{1}{3} \sum_{\gamma=1}^{6} C/A_\gamma + \sum_{k=1}^{3} E_{bending}\,(\theta_{\varsigma\vartheta}) \right]. \tag{2}$$

We defined the expression $\frac{1}{2} \sum_{J=1}^{6} E_{\mathrm{WLC}}(\boldsymbol{r}_{IJ})$in Eq. (2) above as the energy due to the entropic free energy stored in the underlying spectrin protein network, in which the component E_{WLC} is a function of the equilibrium spectrin link length, $\boldsymbol{r}_{IJ}$ and is given by

$$E_{\mathrm{WLC}}(L_i) = \frac{k_B T L_{max} (3x_0^2 - 2x_0^3)}{4p\,(1 - x_0)} \tag{3}$$

where x_0 is the ratio of the maximum contour length to the equilibrium length of the spectrin links, T is the temperature and k_B is the Boltzmann constant with a value of 1.38×10^{-23} J K^{-1}. Secondly, the expression $\frac{1}{3} \sum_{\gamma=1}^{6} C/A_\gamma$ represents the hydrostatic elastic energy stored in the lipid bilayer and other protein materials. A_γ denotes the area of each triangular plaquette in the representative unit cell and C is a constant, calculated using:

$$C = \frac{3\sqrt{3} k_B T L_{max}^3 x_0^4 (4x_0^2 - 9x_0 + 6)}{64p(1 - x_0)^2} \tag{4}$$

Lastly, energy contributions from the bending energy term in Eq. (2) due to the interactions between neighboring triangular plaquettes can be obtained using the expression in Eq. (5) below,

$$E_{bending} = \overline{k}_b \sum_{\langle \varsigma,\vartheta \rangle} [1 - \cos(\theta_{\varsigma\vartheta})], \tag{5}$$

where $\overline{k}_b$ is the RBC membrane bending coefficient, given by $\frac{2k_b}{\sqrt{3}}$, k_b is the bending stiffness of the lipid bilayer, taken to be 2.4×10^{-19} J, and the sum runs over all pairs $\langle \varsigma, \vartheta \rangle$ of neighboring faces of the tessellated membrane surface. $\theta_{\varsigma\vartheta}$ is the instantaneous curvature angles between two neighboring triangles, computed using the surface normal, $\mathbf{n}_\varsigma$ and $\mathbf{n}_\vartheta$, as illustrated in Figure 1 above. The cosine of the instantaneous curvature angle can be computed using the dot product of the normal vectors.

2.3. RBC Membrane Constitutive Relationship

In this subsection, we present a simplified approach to obtain the constitutive responses (namely, the first Piola-Kirchhoff stress tensor and the tangent modulus matrix) of the RBC membrane based on the relationships between the geometry of the representative cell, the strain energy density function expressed in Eq. (2) and the first-order Cauchy-Born rule given in Eq. (1) above.

The first-order Piola-Kirchhoff stress tensor **P** and the tangent modulus matrix **M** are the first- and second-order derivatives of the strain energy density function (W_T) (introduced in the previous subsection) with respect to **Grad**, respectively, and can be calculated using (Xiang & Liew, 2013):

$$\mathbf{P} = \frac{\partial W_T}{\partial \mathbf{Grad}} \text{ and } \quad \mathbf{M} = \frac{\partial^2 W_T}{\partial \mathbf{Grad}^2}. \tag{6}$$

In order to construct the multiscale constitutive relationship for the RBC membrane, we define the coordinates of the junction complexes at the end of the spectrin links in the original reference configuration in vector form as

$$\boldsymbol{R}_{IJ} = (X_1^1, X_2^1, X_3^1, X_1^2, X_2^2, X_3^2, X_1^3, X_2^3, X_3^3, X_1^4, X_2^4, X_3^4, X_1^5, X_2^5, X_3^5, X_1^6, X_2^6, X_3^6)^T, \tag{7}$$

and the coordinates of the junction complexes at the end of the spectrin links in the current configuration after deformation computed using Eq. (1), is stored in vector form as

$$\boldsymbol{r}_{IJ} = (x_1^1, x_2^1, x_3^1, x_1^2, x_2^2, x_3^2, x_1^3, x_2^3, x_3^3, x_1^4, x_2^4, x_3^4, x_1^5, x_2^5, x_3^5, x_1^6, x_2^6, x_3^6)^T. \tag{8}$$

Following the computations above, the deformation gradient tensor and the first-order Piola-Kirchhoff stress tensor are assembled into vector form as follows

$$\mathbf{Grad} = (G_{11}, G_{12}, G_{13}, G_{21}, G_{22}, G_{23}, G_{31}, G_{32}, G_{33})^T, \tag{9}$$

$$\mathbf{P} = (P_{11}, P_{12}, P_{13}, P_{21}, P_{22}, P_{23}, P_{31}, P_{32}, P_{33})^T. \tag{10}$$

Lastly, the stress vector and the tangent modulus matrix can be calculated using the expressions below:

$$\mathbf{P} = \left[\frac{\partial W_T}{\partial \mathbf{Grad}}\right]_{9\times1} = \left[\frac{\partial \mathbf{r}_{IJ}}{\partial \mathbf{Grad}}\right]_{9\times18} \cdot \left[\frac{\partial W_T}{\partial \mathbf{r}_{IJ}}\right]_{18\times1}, \tag{11}$$

$$\mathbf{M} = \left[\frac{\partial^2 W_T}{\partial \mathbf{Grad}^2}\right]_{9\times9} = \left[\frac{\partial \mathbf{r}_{IJ}}{\partial \mathbf{Grad}}\right]_{9\times18} \cdot \left[\frac{\partial^2 W_T}{\partial {\mathbf{r}_{IJ}}^2}\right]_{18\times18} \cdot \left[\frac{\partial \mathbf{r}_{IJ}}{\partial \mathbf{Grad}}\right]^T_{9\times18}. \tag{12}$$

In summary, this section introduces the 3D multiscale hyperelastic constitutive model based on the first-order Cauchy-Born rule, which was used to link the deformation of the atomistic scale representative unit cell of the RBC membrane to the continuum level. The coarse-grained Helmholtz free energy density was then used to define the strain energy density function of the RBC membrane. The current multiscale approach offers several advantages since it avoids the need for empirical constitutive relationship on the macroscale since the precise material properties and constitutive relations are computed directly from the atomistic representative microstructure.

2.4. Nonlinear 3D Multiscale Meshfree Framework

The three-dimensional (3D) nonlinear multiscale meshfree analysis framework for the numerical simulation of the large deformation behavior of RBC membrane in healthy and diseased conditions is presented here. As mentioned previously, the RBC membrane is treated as a 2D surface embedded in a 3D space, therefore, all nodes have three degrees of freedom. For our meshfree computations, the 3D improved moving least-square (IMLS) shape function with the linear basis function and the cubic spline weight functions with a circular support domain were employed (Zhang et al., 2008; Zhang et al., 2019).

The deformation of a material particle $\mathbf{X} \in \Omega_0$ (where Ω_0 denote the region originally occupied by the body) at time t is described by $\mathbf{x}(\mathbf{X}, t)$ through the mapping functions φ is

$$\mathbf{x}(\mathbf{X}, t) = \mathbf{u}(\mathbf{X}, t) + \mathbf{X}, \tag{13}$$

where $\mathbf{u}$ is the displacement of this material particle. The first-order deformation gradients ($\mathbf{Grad}$) can be defined as

$$\mathbf{Grad} = \frac{\partial \mathbf{x}}{\partial \mathbf{X}} = \frac{\partial \mathbf{u}}{\partial \mathbf{X}} + \mathbf{I}. \tag{14}$$

The displacement of the deformed RBC membrane relative to the undeformed RBC membrane when loading is applied can be approximated using

$$\mathbf{u}^h(x) \ = \sum_{i=1}^{N} \phi_i \hat{u}(x_i) = \boldsymbol{\Phi}(\boldsymbol{x})\hat{\mathbf{u}}, \tag{15}$$

where $\hat{\mathbf{u}}$ represents the nodal parameter, ϕ_i denotes the meshfree shape function obtained from the IMLS approximation at the ith node and N is the total number of nodes covered by the compact support domain. For the sake of simplicity, the superscript h in Eq. (15) signifying an approximation is dropped.

The support domain for all the nodes discretizing the problem domain was obtained by first implementing a k-nearest neighbor algorithm to compute the distance between the node of interest and the selected nearest node (d_I). The radius of the support domain (d_{mI}) can therefore be obtained by multiplying the distance, d_I with the meshfree scaling parameter d_{max}.

The first-order deformation gradients ($\mathbf{Grad}$) corresponding to the displacement gradients in Eq. (16) are approximated using Eqs. (14) and (15) as

$$\begin{aligned} \mathbf{Grad} \ &= \sum_{i=1}^{N} \phi_{i,X}\hat{u}_i + \mathbf{I}, \\ &= \sum_{i=1}^{N} [\phi_{i,1} \quad \phi_{i,2} \quad \phi_{i,3}]^T \ \hat{u}_i \ + \mathbf{I}, \end{aligned} \tag{16}$$

where $\phi_{i,X}(X = 1,2,3)$ is the first-order derivative of the meshfree shape function with respect to the original undeformed configuration.

The total energy of the system can be calculated as

$$\prod = \int_{\Omega_0} W_T(\mathbf{Grad}) d\Omega - \int_{\Omega_0} \mathbf{u} \cdot \mathbf{b}_0 d\Omega - \int_{\partial\Omega} \mathbf{u} \cdot \mathbf{t}_0^P dS, \tag{17}$$

where $W_T(\mathbf{Grad})$ is the atomistic scale strain energy density function, computed with the aid of the representative cell as discussed in section 2.2 and $\mathbf{t}_0^P$ represents the first-order stress tractions on the surface of the original domain. Contributions from the body force term ($\mathbf{b}_0$) is neglected. The Ritz parameters are adjusted such that $\delta\Pi = 0$. The weak form of the governing equation can be written as

$$\int_{\Omega_0} \delta \mathbf{Grad}^T \cdot \mathbf{P}\, d\Omega - \int_{\partial\Omega} \delta \mathbf{u}^T \cdot \mathbf{t}_0^P dS = 0. \tag{18}$$

Following the discretization of the nonlinear continuum model in Eq. (18) above, a system of nonlinear algebraic equations is obtained. The use of an iterative procedure is necessary to obtain a solution for such equations. Furthermore, owing to the geometrical nonlinearity and the need to guarantee the second-order convergence rate, a consistent linearization of the weak form is also essential. To achieve this, the vector of unknown stress components at time $t + \Delta t$, denoted by $\mathbf{P}_{n+1}$, is decomposed into a stress vector $\mathbf{P}_n$ at the time t in which the stress components are known, and $\Delta\mathbf{P}_{n+1}$ which contains the hitherto unknown components of the stress increment. The scalar variable t was used as a pseudo-time to parameterize sequences of configurations (i.e. quasi-static deformations).

The stress at the (n+1)th iterative step can be obtained by

$$\mathbf{P}_{n+1} = \mathbf{P}_n + \Delta\mathbf{P}_{n+1}. \tag{19}$$

Substituting the additive decomposition in Eq. (19) above into Eq. (18), the weak equilibrium equation at this iterative step can be rewritten as

$$\int_{\Omega_0} \delta \mathbf{Grad}_{n+1}^T \cdot \Delta\mathbf{P}_{n+1} d\Omega = \int_{\partial\Omega} \delta \mathbf{u}_{n+1}^T \cdot \mathbf{t}_0^P dS - \int_{\Omega_0} \delta \mathbf{Grad}_{n+1}^T \cdot \mathbf{P}_n d\Omega. \tag{20}$$

At the iteration step n+1, by linearizing the equation above (Yan et al., 2012), we obtain Eqs. (21) and (22) below

$$\delta\mathbf{u}_{n+1} = \delta(\mathbf{u}_n + \Delta\mathbf{u}_{n+1}) = \delta\Delta\mathbf{u}_{n+1}, \tag{21}$$

$$\delta\mathbf{Grad}_{n+1} = \delta(\mathbf{Grad}_n + \Delta\mathbf{Grad}_{n+1}) = \delta\Delta\mathbf{Grad}_{n+1}. \tag{22}$$

Based on Eqs. (21) and (22) above, Eq. (20) can be written in the form

$$\int_{\Omega_0} \delta\Delta\mathbf{Grad}_{n+1}^T \cdot \Delta\mathbf{P}_{n+1} d\Omega = \int_{\partial\Omega} \delta\Delta\mathbf{u}_{n+1}^T \cdot \mathbf{t}_0^P dS - \int_{\Omega_0} \delta\Delta\mathbf{Grad}_{n+1}^T \cdot \mathbf{P}_n d\Omega, \tag{23}$$

where $\Delta\mathbf{P}_{n+1} = \mathbf{M} \cdot \Delta\mathbf{Grad}_{n+1}$ and tangent modulus matrix $\mathbf{M}$ is the constitutive material matrix formulated using the first-order Cauchy-Born rule and the atomistic scale strain energy density function. Therefore, Eq. (23) can be rewritten as

$$\int_{\Omega_0} \delta\Delta\mathbf{Grad}_{n+1}^T \cdot \mathbf{M} \cdot \Delta\mathbf{Grad}_{n+1}\, d\Omega = \int_{\partial\Omega} \delta\Delta\mathbf{u}_{n+1}^T \cdot \mathbf{t}_0^P dS - \int_{\Omega_0} \delta\Delta\mathbf{Grad}_{n+1}^T \cdot \mathbf{P}_n d\Omega. \tag{24}$$

The Ritz trial function, which corresponds to the displacement increment ($\Delta\mathbf{u}_{n+1}$) in Eq. (24) of the evaluating point, can be approximated using the IMLS meshfree shape function $\mathbf{\Phi}(\boldsymbol{x})$ and nodal parameter $\Delta\hat{\mathbf{u}}_{n+1}$ as

$$\Delta\mathbf{u}_{n+1} = (\Delta u_1, \Delta u_2, \Delta u_3)^T = \mathbf{\Phi}\Delta\hat{\mathbf{u}}_{n+1}, \tag{25}$$

where

$$\mathbf{\Phi} = \begin{bmatrix} \phi_1 & 0 & 0 & \phi_2 & 0 & 0 & \ddots & & & \phi_N & 0 & 0 \\ 0 & \phi_1 & 0 & 0 & \phi_2 & 0 & & \ddots & & 0 & \phi_N & 0 \\ 0 & 0 & \phi_1 & 0 & 0 & \phi_2 & & & \ddots & 0 & 0 & \phi_N \end{bmatrix}_{(3\times 3N)}, \tag{26}$$

$$\Delta\hat{\mathbf{u}}_{n+1} = [\Delta\hat{u}_{11} \ \ \Delta\hat{u}_{12} \ \ \Delta\hat{u}_{13} \ \ \Delta\hat{u}_{21} \ \ \Delta\hat{u}_{22} \ \ \Delta\hat{u}_{23} \ \ \cdots \ \ \cdots \ \ \cdots \ \ \Delta\hat{u}_{N1} \ \ \Delta\hat{u}_{N2} \ \ \Delta\hat{u}_{N3}\ ]^T_{(1\times 3N)}. \tag{27}$$

Using the IMLS approximation, the deformation gradient increment can be calculated as

$$\Delta\mathbf{Grad}_{n+1} = \mathbf{L}\Delta\mathbf{u}_{n+1} = \mathbf{L}\mathbf{\Phi}\Delta\hat{\mathbf{u}}_{n+1}, \tag{28}$$

where $\mathbf{L}$ is an assembled differential operator matrix with respect to the reference configuration

$$\mathbf{L} = \begin{bmatrix} \frac{\partial}{\partial X_1} & \frac{\partial}{\partial X_2} & \frac{\partial}{\partial X_3} & \mathbf{0} & \mathbf{0} & \mathbf{0} & \mathbf{0} & \mathbf{0} & \mathbf{0} \\ \mathbf{0} & \mathbf{0} & \mathbf{0} & \frac{\partial}{\partial X_1} & \frac{\partial}{\partial X_2} & \frac{\partial}{\partial X_3} & \mathbf{0} & \mathbf{0} & \mathbf{0} \\ \mathbf{0} & \mathbf{0} & \mathbf{0} & \mathbf{0} & \mathbf{0} & \mathbf{0} & \frac{\partial}{\partial X_1} & \frac{\partial}{\partial X_2} & \frac{\partial}{\partial X_3} \end{bmatrix}^{\boldsymbol{T}}. \tag{29}$$

The displacement vector and its variation are approximated by substituting the IMLS shape function into the linearized total energy functional given in Eq. (24) and applying the Ritz minimization procedure (Lim et al., 2005; Zhang et al., 2015) as shown in Eq. (30) below:

$$\frac{\partial\Pi}{\partial\boldsymbol{\eta}} = 0, \ \boldsymbol{\eta} = \Delta\mathbf{u}_i, \quad i = 1, 2, \dots, N. \tag{30}$$

The resulting incremental system equation can be written as

$$\mathbf{K}_{n+1}\Delta\hat{\mathbf{u}}_{n+1} = \mathbf{F}_{n+1}, \tag{31}$$

where $\Delta\hat{\mathbf{u}}_{n+1}$ contains the nodal parameters of all meshfree nodes. $\mathbf{K}_{n+1}$ and $\mathbf{F}_{n+1}$ represent the global stiffness matrix and non-equilibrium force vector, and are expressed as follows

$$\mathbf{K}_{n+1} = \int_{\Omega_0} [(\mathbf{L\Phi})^T \mathbf{M} (\mathbf{L\Phi})\ ] d\Omega, \tag{32}$$

$$\mathbf{F}_{n+1} = \mathbf{F}_{n+1}^{ext} - \mathbf{F}_{n+1}^{int}, \tag{33}$$

where the external force vector $\mathbf{F}_{n+1}^{ext}$ and internal force vector $\mathbf{F}_{n+1}^{int}$ are given by

$$\mathbf{F}_{n+1}^{ext} = \int_{\partial\Omega} \mathbf{\Phi}^T \mathbf{t}_0^P dS, \tag{34}$$

$$\mathbf{F}_{n+1}^{int} = \int_{\Omega_0} (\mathbf{L\Phi})^T \mathbf{P}_n d\Omega. \tag{35}$$

The stiffness matrix in Eq. (32) and the internal force vector in Eq. (35) are integrated using the Gauss quadrature integration technique while the external force vector in Eq. (34) is computed using the direct nodal force application technique. Owing to the computational efficiency of the Newton approach, it was adopted in this study to solve the incremental equilibrium equation, however, the stiffness matrix may become non-positive definite. This drawback can be resolved by simply replacing $\mathbf{K}_{n+1}$ with $\mathbf{K}_{n+1} + \kappa\mathbf{I}_K$, where κ is a positive number that is slightly larger than the magnitude of the most negative eigenvalue of $\mathbf{K}_{n+1}$, and $\boldsymbol{I}_K$ is an identity matrix. After a few cycles of replacements, $\mathbf{K}_{n+1}$ become positive definite and the standard Newton-Raphson method resumes.

3. Results and discussion

3.1. Simulation Procedure

In order to study the large deformation behavior of the RBC membrane in healthy and malaria-infected conditions, we employed the meshfree framework described in section 2.4. above. Here, we simulated the optical tweezers experiment. The optical tweezers experiment is a type of cell stretching experiment in which a single RBC with silica beads attached to its ends is trapped by means of two laser beams. The trapped blood cell is stretched by pulling one of the silica beads, using the laser beam, in the axial direction while the other bead is fixed (Figure 2). The RBC is stretched under the influence of an increasing force, which is dependent on laser power, usually ranging from zero to about 200 picoNewton (pN). Once the cell is stretched, the axial (D_A) and transverse (D_T) diameters, corresponding to the applied stretching force, are recorded.

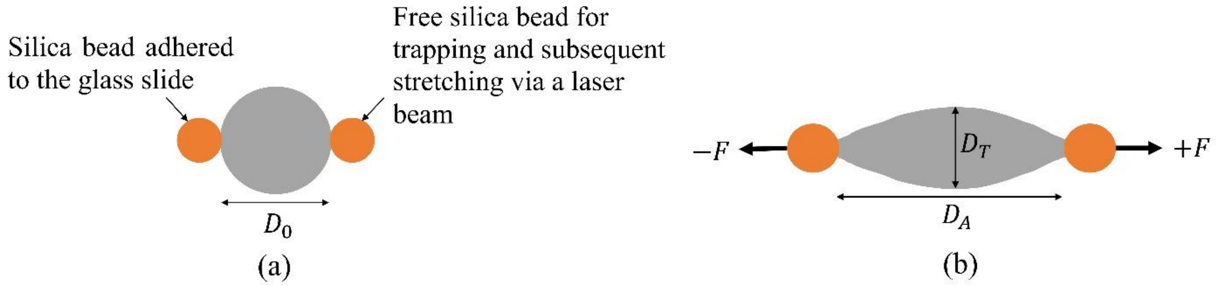

Figure 2. Schematic drawings showing the (a) experimental setup of the optical tweezer with the silica beads attached to the RBC ends, and (b) deformed configuration of the RBC stretched with equal and opposite forces representing the response of the fixed and movable silica beads (Source: Ademiloye et al., 2018, permission requested).

3.2. Simulation Parameters

The normalized geometry of the healthy and malaria-infected RBC membrane, used for numerical simulations in this study, was obtained using the expression in Eq. (36), where x, y and z represent the coordinates of a point cloud representing the RBC surface in a 3D space, while c_0, c_1, and c_2 denote the RBC shape coefficients (Evans and Fung, 1972):

$$z = \pm 0.5 \times \sqrt{1-(x^2+y^2)} \times [c_0 + c_1(x^2+y^2) + c_2(x^2+y^2)^2]. \tag{36}$$

The biconcave RBC geometry was obtained with shape coefficients $c_0 = 0.207$, $c_1 = 2.002$ and $c_2 = -1.123$, while nearly spherical cell geometry was obtained with shape coefficients $c_0 = 1.70$, $c_1 = 0.00$ and $c_2 = 0.00$. The healthy RBC was discretized with $n_m = 162$ meshfree nodes and 766 quadrilateral background cells with four (4) Gauss points in two directions were employed for the numerical integration of Eqs. (32) and (35). For this study, no displacement boundary condition was enforced since the problem domain is a 2D manifold without boundaries, however, in order to ensure that the numerical simulations remain numerically stable and accurate, we applied equal and opposite forces on the two ends of the single cell, following Newton's third law of motion.

Table 1 shows the set of RBC membrane geometry and microstructure parameters employed in our studies. These parameters are dependent on the pathophysiological condition of the cell membrane. It is believed that as the malaria parasite develops the spectrin link length and persistence length, respectively, increases and decreases.

Table 1. Numerical simulation parameters for healthy RBC (hRBC) and malaria-infected RBC (iRBC) membrane in different intraerythrocytic developmental stages, namely ring stage (*Pf*-Rrbc), trophozoite stage (*Pf*-tRBC) and schizont stage (*Pf*-sRBC). (Source: Zhang et al. 2017, permission requested)

Cell condition / infection stage	RBC membrane geometry and microstructure parameters			
	Equilibrium spectrin length, L (nm)	Persistence length, p (nm)	Maximum contour length, L_{max} (nm)	RBC diameter (μm)
hRBC	87.0	8.5	238	7.820
Pf-rRBC	134.85	7.5	238	7.480
Pf-tRBC	139.2	6.0	238	7.260
Pf-sRBC	160.95	4.0	238	7.219

All numerical simulations were computed using our in-house meshfree code developed in MATLAB®. For the meshfree simulations in section 3.3, the following additional parameters were used: bending coefficient, $\bar{k}_b = 2.77 \times 10^{-19} J$, temperature T = 300 K, assumed membrane thickness $h_0 = 12$nm, and meshfree scaling parameter, d_{max} is taken as 1.462. Interested readers are referred to the details presented in Zhang et al. (2017).

3.3. Large Deformation Behavior of RBC membrane in healthy condition

Based on the optical tweezer experiments described in section 3.1, we conducted numerical experiments on healthy and malaria-infected RBCs using our proposed meshfree framework. As shown in Figure 3, the stretching response obtained using our proposed meshfree method is in good agreement with the optical experiments. A comparison between the 3D multiscale meshfree solution and existing methods, namely, spectrin level modeling and the quasi-continuum meshfree simulation, are also presented. This improved prediction can be attributed to the performance of the IMLS meshfree approximation, which requires a smaller number of meshfree nodes in the problem domain and the inclusion of membrane thickness in the formulation (Ademiloye et al., 2018).

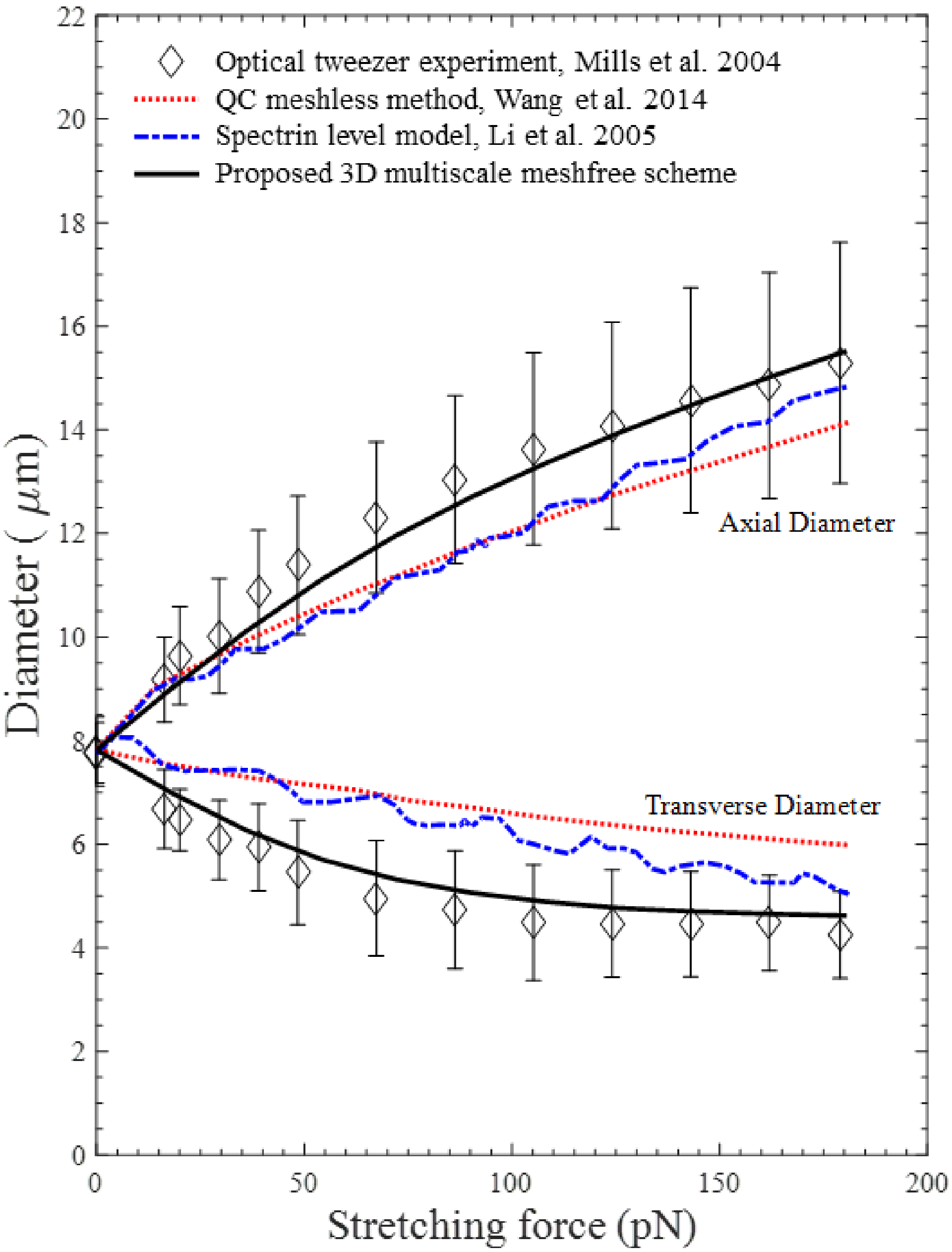

Figure 3. Variations of axial and transverse diameters of the healthy RBC as a function of stretching force in comparison with optical tweezers experiment (Mills et al., 2004), quasi-continuum (QC) meshfree method (Wang et al. 2014), and spectrin level modelling approach (Li et al. 2005). (Source: Ademiloye et al. 2018, permission requested).

The nonlinear formulation employed in the current multiscale meshfree scheme also contributes to its improved prediction, especially in the large deformation region. As shown in Figure 3, our result closely follows the nonlinear trend observed in the experiment and gives better prediction in the large deformation region between 50 pN and 180 pN. Furthermore, the transverse diameter of the RBC membrane was well captured in our numerical experiments in comparison to the other methods. This could be attributed to the inclusion of the precise membrane thickness in our current formulation. It is opined that the current approach to obtain a more realistic prediction of the behavior of RBC membrane in thinner microcapillaries.

We also performed sensitivity analysis on the effect of some important physiological and microstructure parameters, namely temperature, spectrin link length and persistent length. As shown in Figure 4, we can observe that an increase in physiological temperature leads to a corresponding decrease in the deformability of the healthy RBC membrane in terms of its axial and transverse diameter stretch (deformability) decreases. This observation can be attributed to the gradual denaturation of RBC membrane protein with an increase in temperature, thus leading to an increase in the membrane rigidity. Interestingly, we observed that the change in temperature has a more noticeably influence on the axial diameter of the RBC membrane in comparison to that of the transverse diameter. Figure 5 shows that there is an increment in the deformability of the RBC membrane as the initial equilibrium and persistence lengths of the spectrin links increase. This finding is also in complete agreement with the observation in our previous study based on a semi-analytical method (Ademiloye et al. 2015) that the overall rigidity of the RBC membrane decreases with the increase in microstructure parameters especially the persistence length, p.

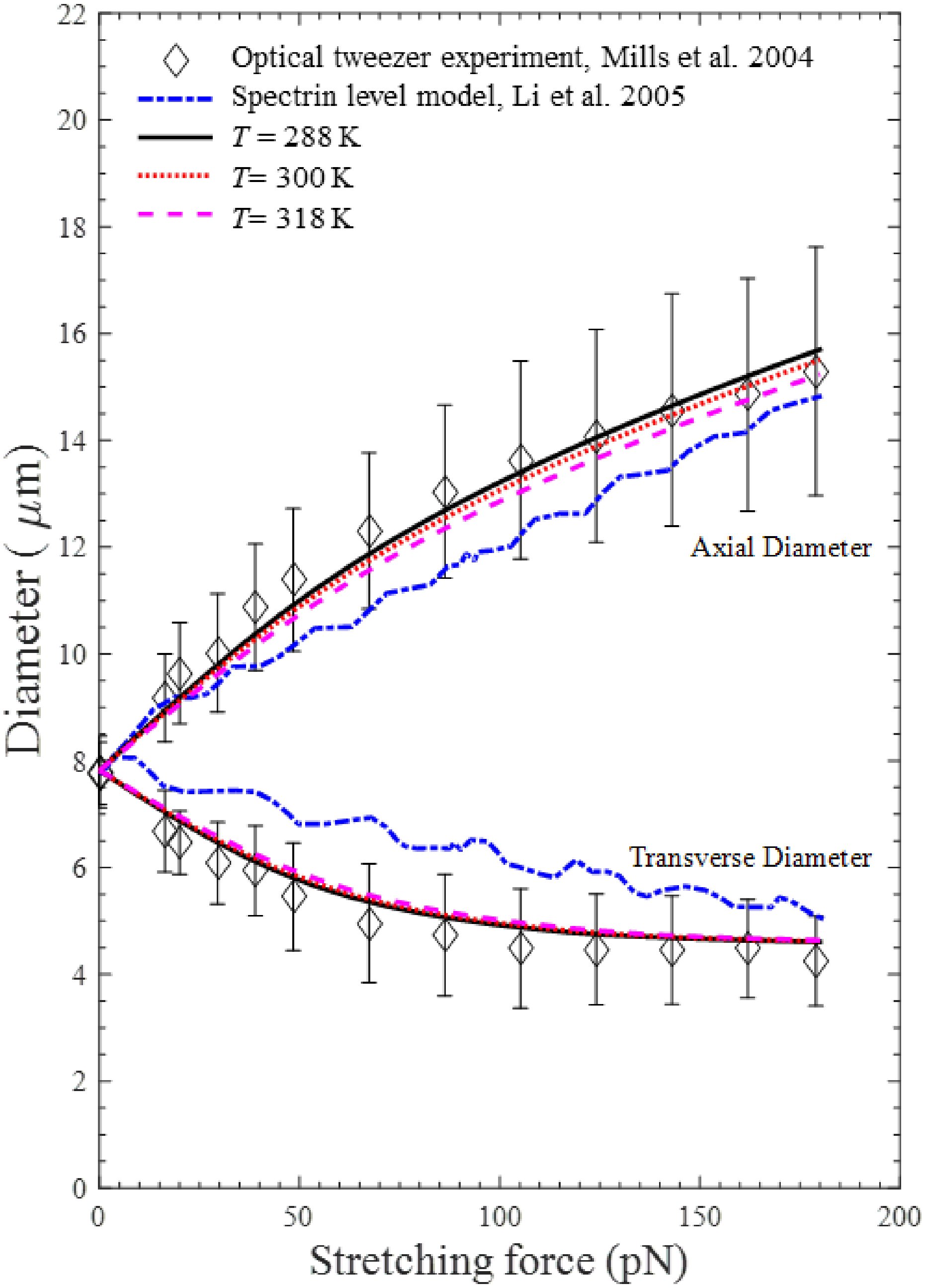

Figure 4. Variations of axial and transverse diameters of the healthy RBC as a function of stretching force using different temperatures in comparison with optical tweezers experiment (Mills et al., 2004), and spectrin level modelling approach (Li et al. 2005) at 300 K. (Source: Ademiloye et al. 2018, permission requested).

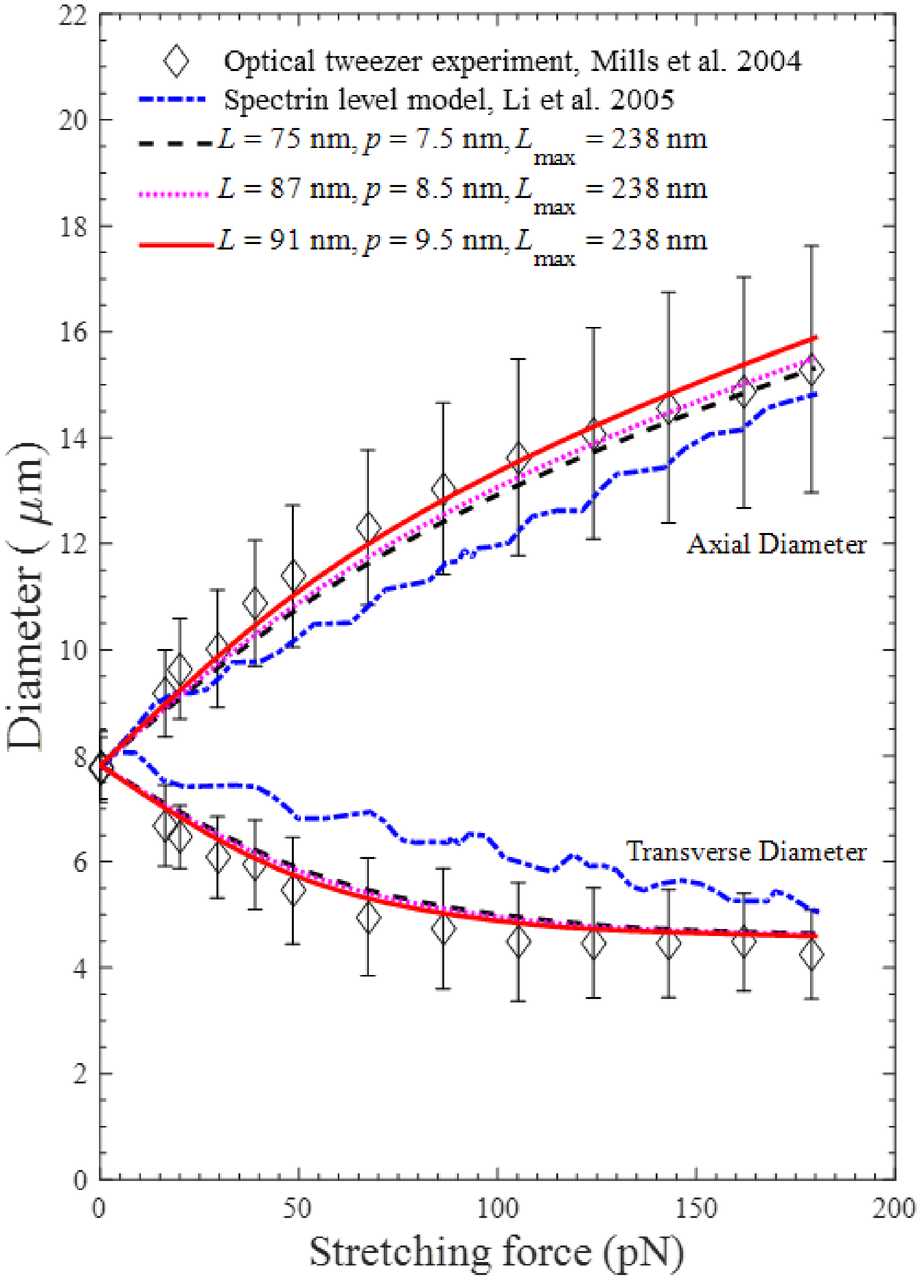

Figure 5. Variations of axial and transverse diameters of the healthy RBC as a function of stretching force using microstructure parameters in comparison with optical tweezers experiment (Mills et al., 2004), and spectrin level modelling approach (Li et al. 2005) at 300 K. (Source: Ademiloye et al. 2018, permission requested).

3.4. Numerical Study on the Large Deformation Behavior of Malaria-Infected Red Blood Cell Membrane

As previously stated, it has been widely established that the deformability of RBC membrane is reduced in malaria-infection. Of all four known species of malaria parasite that infect humans, *Plasmodium (P.) falciparum* has been identified as the most prevalent and lethal malaria parasite (Udeinya et al., 1981). Malaria-infected RBCs (iRBCs) progressively lose their deformability as well as the ability to recover their biconcave shape as the merozoites mature during the different intraerythrocytic developmental stages, namely ring stage (*Pf*-rRBC), trophozoite stage (*Pf*-tRBC) and schizont stage (*Pf*-sRBC), resulting in a significant increase in shear modulus, rigidity and cell viscosity (Suresh, 2006). Using the technique described in section 3.1, the large deformation behavior of iRBC membrane was investigated by means of numerical simulation of the optical tweezer experiments. The pathophysiological parameters representing the iRBC membrane in our constitutive model as the malaria-infection progresses are presented in Table 1.

Based on the optical tweezer experiments (as shown in Figure 2), the relationship between varying applied stretching force and changes in axial and transverse diameters of iRBC membrane in *Pf*-rRBC, *Pf*-tRBC and *Pf*-sRBC stages are shown in Figures 6, 7 and 8, respectively. These numerical results are also presented in comparison with experimental and numerical results in the literature. Our results obtained using a multiscale meshfree simulation agree well with the experimental results and data in the literature (Suresh et al., 2005).

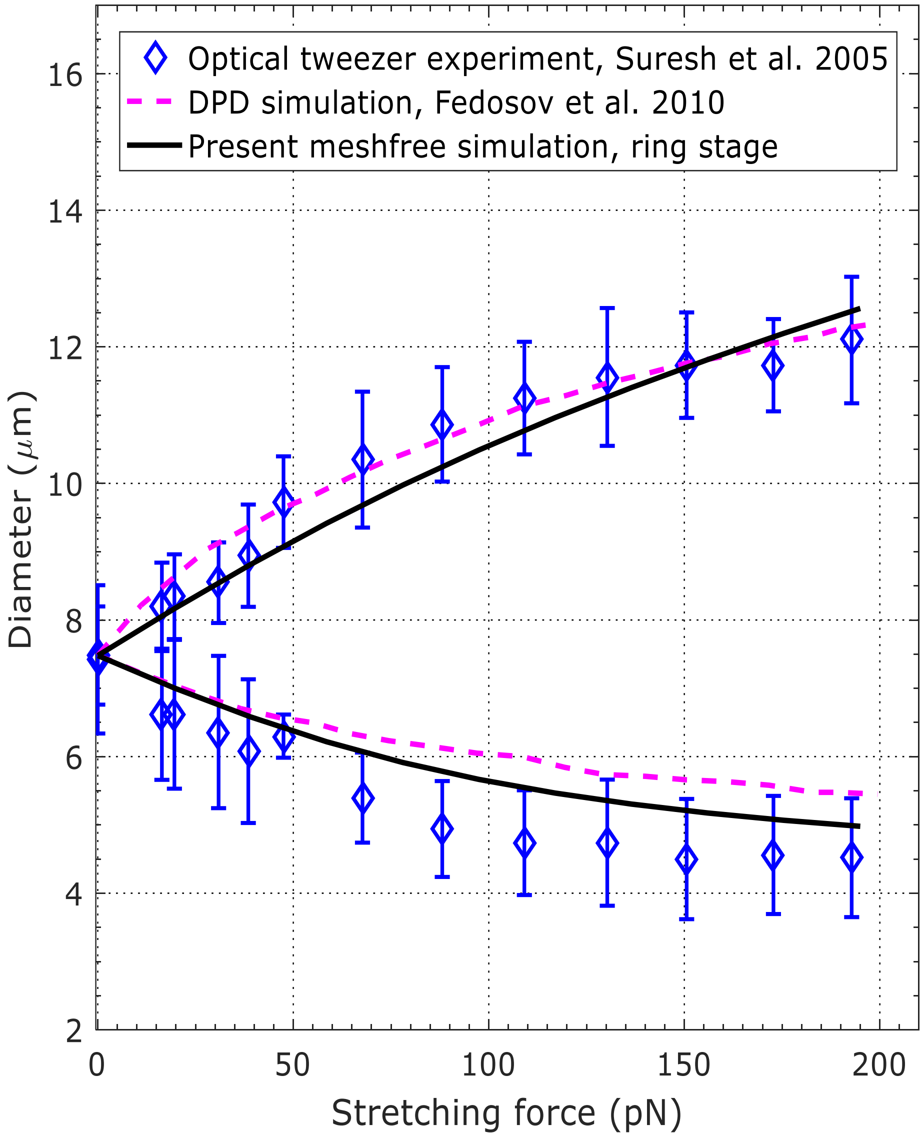

Figure 6. Variations of axial and transverse diameters of a malaria-infected RBC membrane during the ring stage (*Pf*-rRBC) as a function of stretching force in comparison with experimental data (Suresh et al., 2005) and DPD simulations (Fedosov et al., 2010). (Source: Zhang et al. 2017, permission requested).

Although it has been suggested in literature that the morphology of RBCs changes from biconcave to nearly spherical shape as malaria infection progresses, a comparison between the numerical results obtained using a biconcave and nearly spherical geometry are presented in Figures 7 and 8 for the trophozoite and schizont infection stages. Our numerical results show that a more accurate prediction of the large deformation behaviors of the iRBC membrane in terms of its transverse diameter can be obtained if the cell geometry is assumed to remain biconcave as infection progresses. Here, we suggest that since the precise shape of iRBC membranes can vary significantly, the biconcave cell geometry, which is well established and known, should be employed for numerical simulations to minimize the error associated with geometry uncertainty. Furthermore, by using the current multiscale modelling approach, computational errors associated with the assumption of iRBC membrane properties such as Young's modulus and shear modulus as well as problem domain approximation can be avoided since the constitutive responses of the iRBC membrane were computed from the microstructure parameters of the spectrin network rather than assumed material properties.

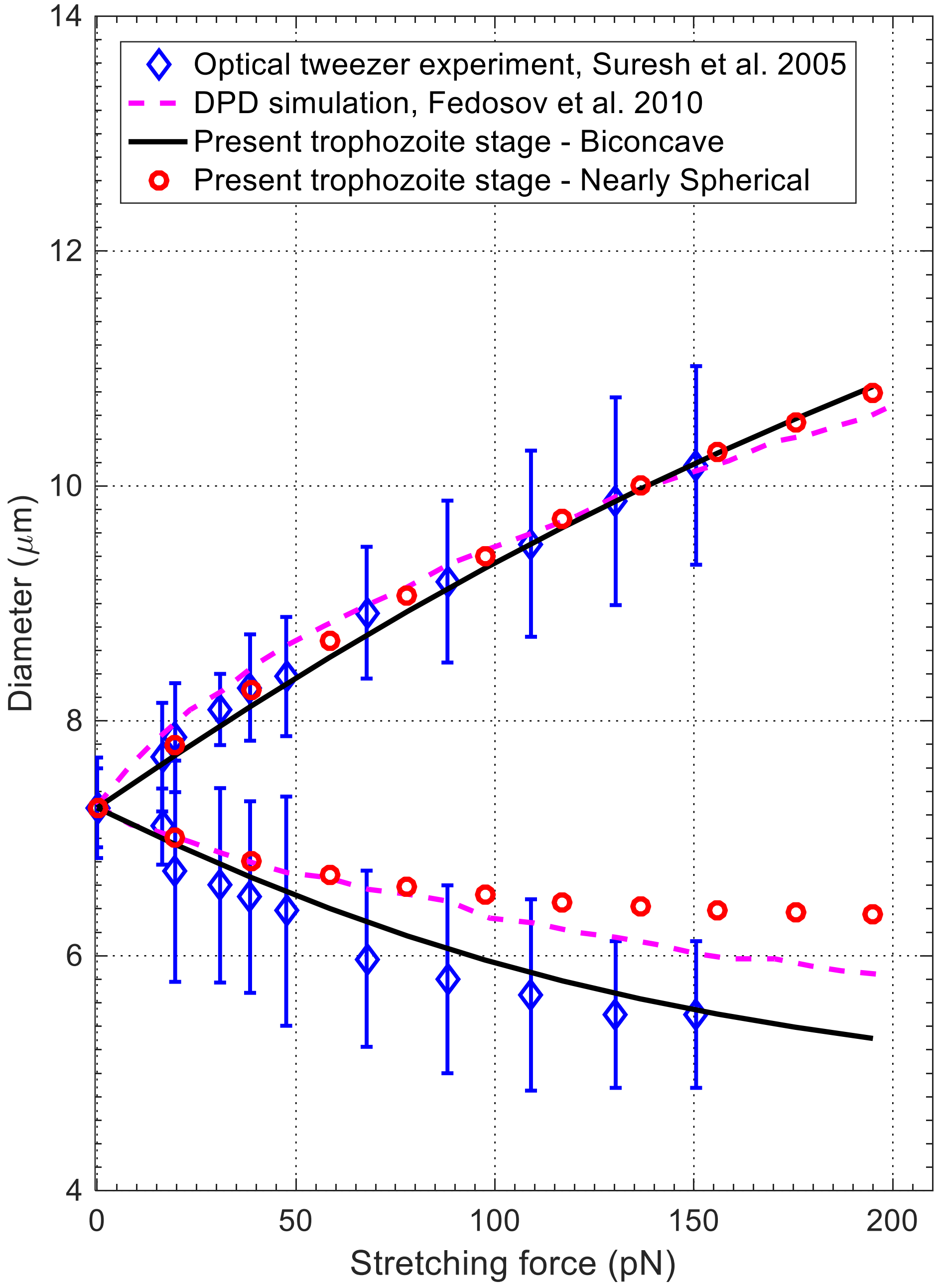

Figure 7. Force-diameter curve of the malaria-infected RBC membrane during the trophozoite (*Pf*-tRBC) stage obtained using biconcave and nearly spherical cell geometries in comparison with experimental data (Suresh et al., 2005) and DPD simulations (Fedosov et al., 2010). (Source: Zhang et al. 2017, permission requested).

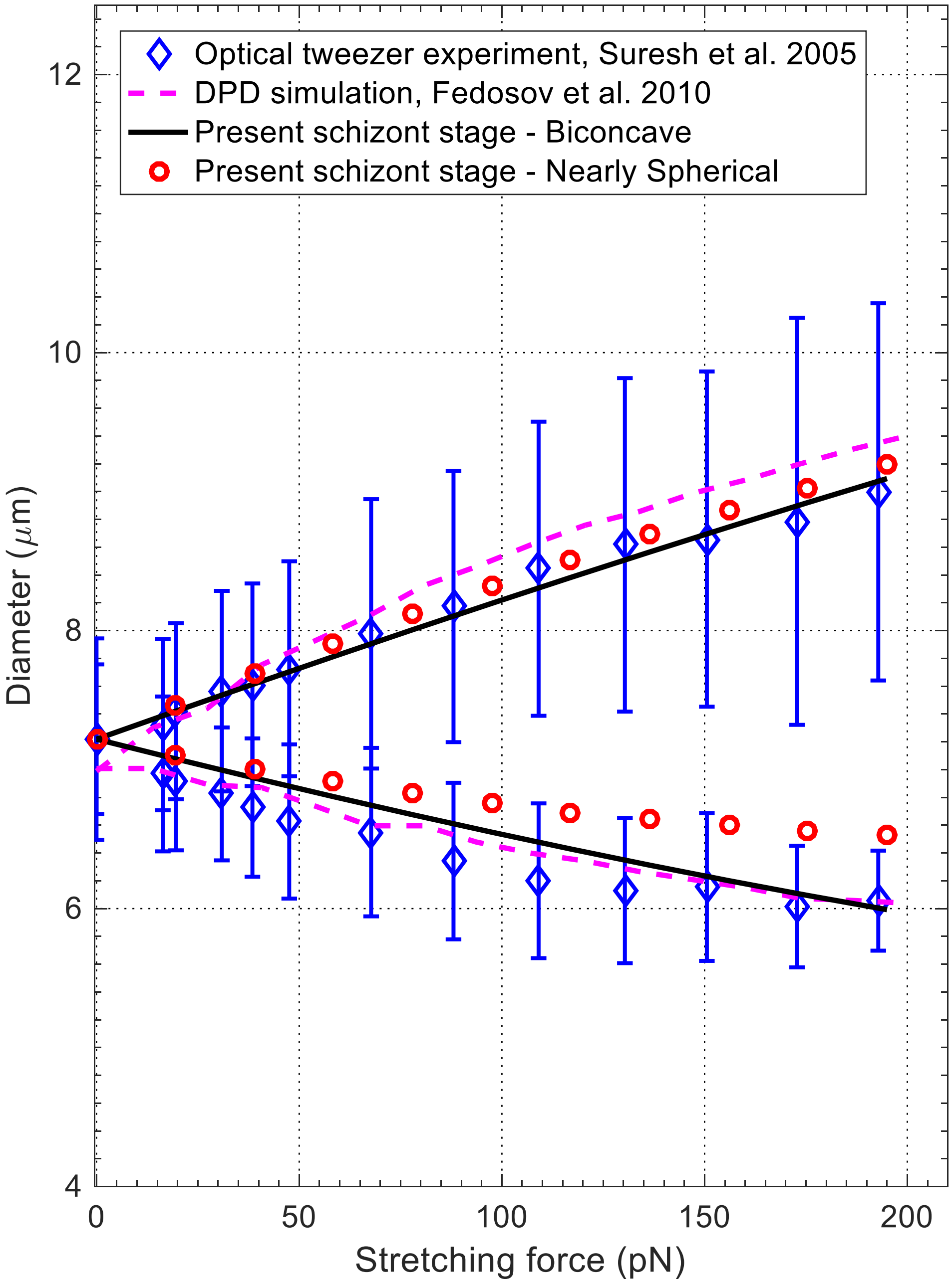

Figure 8. Force-diameter curve of the malaria-infected RBC membrane during the schizont (*Pf*-sRBC) stage obtained using biconcave and nearly spherical cell geometries in comparison with experimental data (Suresh et al., 2005) and DPD simulations (Fedosov et al., 2010). (Source: Zhang et al. 2017, permission requested).

4. Concluding Remarks and Prospects

In this chapter, a meshfree multiscale modelling technique for investigating the biomechanical properties of human red blood cells (RBCs) is presented. This approach combines the accuracy of atomistic level modelling by accounting for microscopic properties of RBC membrane in healthy and diseased conditions as well as the reduced computational cost associated with continuum level modelling. Furthermore, the precise effect of membrane thickness is directly incorporated into the formulation, thus ensuring that the RBC membrane is correctly treated as a 2D surface in a 3D space. The results obtained using the current approach are in excellent agreement with experimental studies in literature and it provides specific insights into the precise influence of microstructural alterations on the macroscale behavior of RBCs during large deformation.

Despite the overall advantages of the proposed multiscale technique, there are several opportunities for further developments. For instance, the current approach is purely mechanistic, which must be coupled with appropriate kinetic models in order to provide insights into the influence of biochemical alterations on the deformability of RBCs in metabolic diseases such as Type 2 diabetes mellitus. Moreover, the improved element-free Galerkin method employed in the current formulation could limit the use of the multiscale technique for studying RBC dynamics in blood flow. Meshfree methods are generally more computationally expensive due to their shape function construction cost. In addition to this, the essential boundary conditions in meshfree methods cannot be directly imposed as in the finite element method without additional intervention due to their lack of Kronecker delta property.

Finally, the construction of a linkage between the atomistic and continuum levels was obtained using the first-order Cauchy−Born rule, which depends on the deformation gradient of the representative unit cell. The higher-order Cauchy−Born rule could be employed to correctly describe the bending effect and buckling deformation of the membrane (Ademiloye et al., 2015; Sunyk & Steinmann, 2003). Furthermore, the use of machine learning could be employed to explore the linkage between different scales and predict the behavior of RBCs in different pathological conditions, if there is enough data available. By combining machine learning with multiscale modelling (Nguyen et al., 2023), new insights in terms of features and correlations across different scales can be obtained and the cost of computations can be reduced using surrogate models for approximation of complex simulations. This combination could create a pathway for improved diagnostics as well as the development of new therapeutics for RBC-related disorders.

References

Ademiloye, A. S., Zhang, L. W., & Liew, K. M. (2015). Numerical computation of the elastic and mechanical properties of red blood cell membrane using the higher-order Cauchy–Born rule. Applied Mathematics and Computation, 268, 334–353. https://doi.org/10.1016/j.amc.2015.06.071

Ademiloye, A. S. (2017). Development of a Multiscale Cauchy-Born Framework for Modeling the Biomechanical Properties of Healthy and Malaria-infected Red Blood Cell Membrane (Doctoral dissertation, City University of Hong Kong).

Ademiloye, A. S., Zhang, L. W., & Liew, K. M. (2017). Atomistic–continuum model for probing the biomechanical properties of human erythrocyte membrane under extreme conditions. Computer Methods in Applied Mechanics and Engineering, 325, 22–36. https://doi.org/10.1016/j.cma.2017.06.033

Ademiloye, A. S., Zhang, L. W., & Liew, K. M. (2018). A multiscale framework for large deformation modeling of RBC membranes. Computer Methods in Applied Mechanics and Engineering, 329, 144–167. https://doi.org/10.1016/j.cma.2017.10.004

Ahmadian, M.T., Firoozbakhsh, K., & Hasanian, M. (2011). Simulation of red blood cell motion in microvessels using modified moving particle semi-implicit method. Scientia Iranica, 19, 113-118. https://doi.org/10.1016/j.scient.2011.12.007

Chien, S., Sung, K. L., Skalak, R., Usami, S., & Tözeren, A. (1978). Theoretical and experimental studies on viscoelastic properties of erythrocyte membrane. Biophysical Journal, 24(2), 463–487. https://doi.org/10.1016/S0006-3495(78)85395-8

Cranston, H.A., Boylan, C.W., Carroll, G.L., Sutera, S.P., Williamson, J.R., Gluzman, I.Y. and Krogstad, D.J. (1984). Plasmodium falciparum maturation abolishes physiologic red cell deformability. Science, 223, 400–403. doi:10.1126/science.6362007.

Dao, M., Li, J., & Suresh, S. (2006). Molecularly based analysis of deformation of spectrin network and human erythrocyte. Materials Science and Engineering C, 26(8), 1232–1244. https://doi.org/10.1016/j.msec.2005.08.020

Dao, M., Lim, C. T., & Suresh, S. (2003). Mechanics of the human red blood cell deformed by optical tweezers. Journal of the Mechanics and Physics of Solids, 51(11), 2259–2280. https://doi.org/10.1016/j.jmps.2003.09.019

Discher, D.E., Boey, S.K., & Boal, D.H. (1998). Simulations of the erythrocyte cytoskeleton at large deformation. I. Microscopic models. Biophysical Journal, 75, 1573–83. https://doi.org/10.1016/S0006-3495(98)74075-5.

Dulińska, I., Targosz, M., Strojny, W., Lekka, M., Czuba, P., Balwierz, W., & Szymoński, M. (2006). Stiffness of normal and pathological erythrocytes studied by means of atomic force microscopy. Journal of Biochemical and Biophysical Methods, 66(1–3), 1–11. https://doi.org/10.1016/j.jbbm.2005.11.003

Dupin, M., Halliday, I., Care, C., Alboul, L., & Munn, L. (2007). Modeling the flow of dense suspensions of deformable particles in three dimensions. Physical Review E, 75(6), 066707. https://doi.org/10.1103/PhysRevE.75.066707

Evans, E. A. (1973). New membrane concept applied to the analysis of fluid shear- and micropipette-deformed red blood cells. Biophysical Journal, 13(9), 941–954. https://doi.org/10.1016/S0006-3495(73)86036-9

Evans, E., & Fung, Y.C., (1972). Improved measurements of the erythrocyte geometry. Microvasc. Res. 4, 335–347. doi:10.1016/0026-2862(72)90069-6.

Fedosov, D.A., Caswell, B., & Karniadakis, G. E. (2010). Systematic coarse-graining of spectrin-level red blood cell models. Computer Methods in Applied Mechanics and Engineering, 199(29), 1937–1948. https://doi.org/10.1016/j.cma.2010.02.001

Fedosov, D.A., Lei, H., Caswell, B., Suresh, S., & Karniadakis, G.E. (2011). Multiscale modeling of red blood cell mechanics and blood flow in malaria, PLoS Computational Biology 7. https://doi.org/10.1371/journal.pcbi.1002270.

Fedosov, D.A., Noguchi, H., & Gompper, G. (2014). Multiscale modeling of blood flow: From single cells to blood rheology. Biomechanics and Modeling in Mechanobiology, 13(2), 239–258. https://doi.org/10.1007/s10237-013-0497-9

Franke, T., Hoppe, R. H. W., Linsenmann, C., Schmid, L., Willbold, C., & Wixforth, A. (2011). Numerical simulation of the motion of red blood cells and vesicles in microfluidic flows. Computing and Visualization in Science, 14(4), 167–180. https://doi.org/10.1007/s00791-012-0172-1

Hansen, J.C., Skalak, R., Chien, S. & Hoger, A. (1996). An elastic network model based on the structure of the red blood cell membrane skeleton. Biophysical Journal, 70, 146–66. https://doi.org/10.1016/S0006-3495(96)79556-5

Hartmann, D. (2010). A multiscale model for red blood cell mechanics. Biomechanics and Modeling in Mechanobiology, 9, 1-17. https://doi.org/10.1007/s10237-009-0154-5

Henon, S., Lenormand, G., Richert, A., & Gallet, F. (1999). A new determination of the shear modulus of the human erythrocyte membrane using optical tweezers. Biophysical Journal, 76, 1145–1151.

Hosseini, S. M., & Feng, J. J. (2009). A particle-based model for the transport of erythrocytes in capillaries. Chemical Engineering Science, 64(22), 4488–4497. https://doi.org/10.1016/j.ces.2008.11.028

Imai, Y., Omori, T. Shimogonya, Y., Yamaguchi, T. & Ishikawa, T. (2016). Numerical methods for simulating blood flow at macro, micro, and multiscales. Journal of Biomechanics, 49, 2221-2228.

Klöppel, T., & Wall, W. A. (2011). A novel two-layer, coupled finite element approach for modeling the nonlinear elastic and viscoelastic behavior of human erythrocytes. Biomechanics and Modeling in Mechanobiology, 10(4), 445–459. https://doi.org/10.1007/s10237-010-0246-2

Krüger, T. Varnik, F. & Raabe, D. (2011). Efficient and accurate simulations of deformable particles immersed in a fluid using a combined immersed boundary lattice Boltzmann finite element method. Computers & Mathematics with Applications, 61, 3485–3505. https://doi.org/10.1016/j.camwa.2010.03.057.

Krüger, T. (2012). Computer simulation study of collective phenomena in dense suspensions of red blood cells under shear. Springer Spektrum. https://doi.org/10.1007/978-3-8348-2376-2

Krüger, T., Gross, M., Raabe, D., & Varnik, F. (2013). Crossover from tumbling to tank-treading-like motion in dense simulated suspensions of red blood cells. Soft Matter, 9(37), 9008–9015. https://doi.org/10.1039/C3SM51645H

Krüger, T., Kaoui, B., & Harting, J. (2014). Interplay of inertia and deformability on rheological properties of a suspension of capsules. Journal of Fluid Mechanics, 751, 725–745. https://doi.org/10.1017/jfm.2014.315

Kuznetsova, T. G., Starodubtseva, M. N., Yegorenkov, N. I., Chizhik, S. A., & Zhdanov, R. I. (2007). Atomic force microscopy probing of cell elasticity. Micron, 38(8), 824–833. https://doi.org/10.1016/j.micron.2007.06.011

Lee, J. C., & Discher, D. E. (2001). Deformation-Enhanced Fluctuations in the Red Cell Skeleton with Theoretical Relations to Elasticity , Connectivity , and Spectrin Unfolding Theoretical Relations to Elasticity , Connectivity , and Spectrin Unfolding. Biophysical Journal, 81(6), 3178–3192.

Lenormand, G., Hénon, S., Richert, A., Siméon, J., & Gallet, F. (2001). Direct measurement of the area expansion and shear moduli of the human red blood cell membrane skeleton. Biophysical Journal, 81(1), 43–56. https://doi.org/10.1016/S0006-3495(01)75678-0

Li, J., Dao, M., Lim, C. T., & Suresh, S. (2005). Spectrin-Level Modeling of the Cytoskeleton and Optical Tweezers Stretching of the Erythrocyte. Biophysical Journal, 88(5), 3707–3719. https://doi.org/10.1529/biophysj.104.047332

Ma, S., Wang, S., Qi, X., Han, K., Jin, X., Li, Z., Hu, G. & Li, X. (2022). Multiscale computational framework for predicting viscoelasticity of red blood cells in aging and mechanical fatigue. Computer Methods in Applied Mechanics and Engineering, 391, 114535. https://doi.org/10.1016/j.cma.2021.114535

McWhirter, J. L., Noguchi, H., & Gompper, G. (2012). Ordering and arrangement of deformed red blood cells in flow through microcapillaries. New Journal of Physics, 14. https://doi.org/10.1088/1367-2630/14/8/085026

Mills, J. P., Qie, L., Dao, M., Lim, C. T., & Suresh, S. (2004). Nonlinear elastic and viscoelastic deformation of the human red blood cell with optical tweezers. Mechanics & Chemistry of Biosystems : MCB, 1(3), 169–180.

Nguyen, P. C. H., Choi, J. B., Udaykumar, H. S., & Baek, S. (2023). Challenges and opportunities for machine learning in multiscale computational modeling. Journal of Computing and Information Science in Engineering, *23*(6), 060808.

Noguchi, H. (2009). Membrane simulation models from nanometer to micrometer scale. Journal of the Physical Society of Japan, 78(4), 1–9. https://doi.org/10.1143/JPSJ.78.041007

Noguchi, H. (2010). Dynamical modes of deformed red blood cells and lipid vesicles in flows. Progress of Theoretical Physics Supplement, 184(184), 364–368. https://doi.org/10.1143/PTPS.184.364

Noguchi, H., & Gompper, G. (2005). Shape transitions of fluid vesicles and red blood cells in capillary flows. Proceedings of the National Academy of Sciences of the United States of America, 102(40), 14159–14164. https://doi.org/10.1073/pnas.0504243102

Noguchi, H., & Gompper, G. (2006). Meshless membrane model based on the moving least-squares method. Physical Review E - Statistical, Nonlinear, and Soft Matter Physics, 73(2), 1–12. https://doi.org/10.1103/PhysRevE.73.021903

Pan, L., Yan, R., Li, W. and Xu, K. (2018). Super-Resolution Microscopy Reveals the Native Ultrastructure of the Erythrocyte Cytoskeleton, Cell Reports, 22(5), 1151-1158. https://doi.org/10.1016/j.celrep.2017.12.107.

Pivkin, I., & Karniadakis, G. (2008). Accurate coarse-grained modeling of red blood cells. Physical Review Letters, 101(11), 118105. https://doi.org/10.1103/PhysRevLett.101.118105

Quinn, D. J., Pivkin, I., Wong, S. Y., Chiam, K. H., Dao, M., Karniadakis, G. E., & Suresh, S. (2011). Combined simulation and experimental study of large deformation of red blood cells in microfluidic systems. Annals of Biomedical Engineering, 39(3), 1041–1050. https://doi.org/10.1007/s10439-010-0232-y

Rancourt-Grenier, S., Wei, M.-T., Bai, J.-J., Chiou, A., Bareil, P. P., Duval, P.-L., & Sheng, Y. (2010). Dynamic deformation of red blood cell in dual-trap optical tweezers. Optics Express, 18(10), 10462–10472. https://doi.org/10.1364/OE.18.010462

Strey, H., Peterson, M., & Sackmann, E. (1995). Measurement of erythrocyte membrane elasticity by flicker eigenmode decomposition. Biophysical Journal, 69(2), 478–488. https://doi.org/10.1016/S0006-3495(95)79921-0

Sunyk, R., & Steinmann, P. (2003). On higher gradients in continuum-atomistic modelling. International Journal of Solids and Structures, 40(24), 6877-6896.

Suresh, S., Spatz, J., Mills, J. P., Micoulet, A., Dao, M., Lim, C. T., Beil, M. & Seufferlein, T. (2005). Connections between single-cell biomechanics and human disease states: gastrointestinal cancer and malaria. Acta Biomaterialia, 1, 15-30. https://doi.org/10.1016/j.actbio.2004.09.001

Suresh, S. (2006). Mechanical response of human red blood cells in health and disease: Some structure-property-function relationships. Journal of Materials Research, 21(8), 1871-1877. doi:10.1557/jmr.2006.0260.

Tadmor, E. B., Smith, G. S., Bernstein, N., & Kaxiras, E. (1999). Mixed finite element and atomistic formulation for complex crystals. Physical Review B, 59(1), 235. doi:10.1103/PhysRevB.59.235.

Tan, Y., Sun, D., Huang, W., & Li, H. (2009). Mechanical characterization of human red blood cells by robotic manipulation with optical tweezers. Robotics and Biomimetics (ROBIO), 2009 IEEE International Conference On, 57(7), 1816–1825. https://doi.org/10.1109/ROBIO.2009.5420707

Tsubota, K., Wada, S. & Yamaguchi, T., (2006). Particle method for computer simulation of red blood cell motion in blood flow. Computer Methods and Programs in Biomedicine, 83, 139–146. https://doi.org/10.1016/j.cmpb.2006.06.005.

Udeinya, I.J., Schmidt, J.A., Aikawa, M., Miller, L.H., Green, I., (1981). Falciparum malaria infected erythrocytes specifically bind to cultured human endothelial cells. Science 213, 555–557.

Wang, X. Y., Guo, X., & Su, Z. (2014). A quasi-continuum model for human erythrocyte membrane based on the higher order Cauchy–Born rule. Computer Methods in Applied Mechanics and Engineering, 268, 284–298. https://doi.org/10.1016/j.cma.2013.08.020

World Health Organization. (2024). World malaria report 2024. World Health Organization.

Xiang, P., & Liew, K. M. (2013). A computational framework for transverse compression of microtubules based on a higher-order Cauchy–Born rule. *Computer Methods in Applied Mechanics and Engineering*, *254*, 14-30. https://doi.org/10.1016/j.cma.2012.10.013

Yu, L., Sheng, Y., & Chiou, A. (2013). Three-dimensional light-scattering and deformation of individual biconcave human blood cells in optical tweezers. Optics Express, 21(10), 12174–12184. https://doi.org/10.1364/OE.21.012174

Yan, J.W., Liew, K.M., & He, L.H. (2012). A mesh-free computational framework for predicting buckling behaviors of single-walled carbon nanocones under axial compression based on the moving Kriging interpolation. Comput. Methods Appl. Mech. Eng. 247-248 (2012) 103–112. doi:10.1016/j.cma.2012.08.010.

Zhang, L. W., Ademiloye, A. S., & Liew, K. M. (2017). A multiscale Cauchy–Born meshfree model for deformability of red blood cells parasitized by Plasmodium falciparum. Journal of the Mechanics and Physics of Solids, 101, 268-284.

Zhang, L. W., Ademiloye, A. S., & Liew, K. M. (2019). Meshfree and particle methods in biomechanics: Prospects and challenges. Archives of Computational Methods in Engineering, 26(5), 1547-1576.

Zhang, Z., Liew, K.M., Cheng, Y., Lee, Y.Y. (2008). Analyzing 2D fracture problems with the improved element-free Galerkin method. Eng. Anal. Bound. Elem. 32, 241–250. doi:10.1016/j.enganabound.2007.08.012